

## Article

# Fe<sub>2</sub>O<sub>3</sub> Nanoparticles Deposited over Self-Floating Facial Sponge for Facile Interfacial Seawater Solar Desalination

Yuzheng Lu <sup>1</sup>, Naila Arshad <sup>2</sup>, Muhammad Sultan Irshad <sup>3,\*</sup>, Iftikhar Ahmed <sup>4,\*</sup>, Shafiq Ahmad <sup>5</sup>, Lina Abdullah Alshahrani <sup>6</sup>, Muhammad Yousaf <sup>7</sup>, Abdelaty Edrees Sayed <sup>5</sup> and Muhammad Nauman <sup>8</sup>

<sup>1</sup> School of Electronic Engineering, Nanjing Xiaozhuang University, Nanjing 211171, China; mrluyuzheng@163.com

<sup>2</sup> Institute of Quantum Optics and Quantum Information, School of Science, Xi'an Jiaotong University (XJTU), Xi'an 710049, China; nailasehar371@gmail.com

<sup>3</sup> School of Materials Science and Engineering, Hubei University, Wuhan 430062, China

<sup>4</sup> ERC Research Centre, COMSATS University Islamabad, Lahore Campus, Islamabad 54000, Pakistan

<sup>5</sup> Industrial Engineering Department, College of Engineering, King Saud University, P.O. Box 800, Riyadh 11421, Saudi Arabia; ashafiq@ksu.edu.sa (S.A.); aesayed@ksu.edu.sa (A.E.S.)

<sup>6</sup> School of Chemistry & Environment, South China Normal University, Guangzhou 510006, China; Lamy7667@hotmail.com

<sup>7</sup> School of Energy and Environment, Southeast University, Nanjing 210096, China; tahayousaf@gmail.com

<sup>8</sup> Institute of Science and Technology (IST), 3400 Klosterneuburg, Austria; muhammad.nauman@ist.ac.at

\* Correspondence: sultan.danish93@gmail.com (M.S.I.); dr.Iftikhar.Ahmed@live.fr (I.A.); Tel.: +86-15623138982 (M.S.I.); +92-3218856761 (I.A.)



**Citation:** Lu, Y.; Arshad, N.; Irshad, M.S.; Ahmed, I.; Ahmad, S.; Alshahrani, L.A.; Yousaf, M.; Sayed, A.E.; Nauman, M. Fe<sub>2</sub>O<sub>3</sub> Nanoparticles Deposited over Self-Floating Facial Sponge for Facile Interfacial Seawater Solar Desalination. *Crystals* **2021**, *11*, 1509. <https://doi.org/10.3390/cryst11121509>

Academic Editors: David Holec and Efrém Curcio

Received: 3 November 2021

Accepted: 29 November 2021

Published: 3 December 2021

**Publisher's Note:** MDPI stays neutral with regard to jurisdictional claims in published maps and institutional affiliations.



**Copyright:** © 2021 by the authors. Licensee MDPI, Basel, Switzerland. This article is an open access article distributed under the terms and conditions of the Creative Commons Attribution (CC BY) license (<https://creativecommons.org/licenses/by/4.0/>).

**Abstract:** A facile approach for developing an interfacial solar evaporator by heat localization of solar-thermal energy conversion at water-air liquid composed by in-situ polymerization of Fe<sub>2</sub>O<sub>3</sub> nanoparticles (Fe<sub>2</sub>O<sub>3</sub>@PPy) deposited over a facial sponge is proposed. The demonstrated system consists of a floating solar receiver having a vertically cross-linked microchannel for wicking up saline water. The in situ polymerized Fe<sub>2</sub>O<sub>3</sub>@PPy interfacial layer promotes diffuse reflection and its rough black surface allows Omni-directional solar absorption (94%) and facilitates efficient thermal localization at the water/air interface and offers a defect-rich surface to promote heat localization (41.9 °C) and excellent thermal management due to cellulosic content. The self-floating composite foam reveals continuous vapors generation at a rate of 1.52 kg m<sup>-2</sup> h<sup>-1</sup> under one 1 kW m<sup>-2</sup> and profound evaporating efficiency (95%) without heat losses that dissipates in its surroundings. Indeed, long-term evaporation experiments reveal the negligible disparity in continuous evaporation rate (33.84 kg m<sup>-2</sup>/8.3 h) receiving two sun solar intensity, and ensures the stability of the device under intense seawater conditions synchronized with excellent salt rejection potential. More importantly, Raman spectroscopy investigation validates the orange dye rejection via Fe<sub>2</sub>O<sub>3</sub>@PPy solar evaporator. The combined advantages of high efficiency, self-floating capability, multimedia rejection, low cost, and this configuration are promising for producing large-scale solar steam generating systems appropriate for commercial clean water yield due to their scalable fabrication.

**Keywords:** in-situ polymerization; Fe<sub>2</sub>O<sub>3</sub>; facial sponge; solar evaporation; desalination

## 1. Introduction

Freshwater scarcity has emerged as a serious global challenge, which can endanger the survival of all of the species in the hemisphere. Although 70% of our planet's area is covered by water, unfortunately only 3% comprises freshwater, of which 66% is unavailable due to glaciers and frozen lakes, ice caps, and being underground [1,2]. Ever-increasing industrial growth, urbanization, climate change, and population growth have made the availability of freshwater an unprecedented challenge to mankind [3]. Existing technologies such as membrane-based (reverse osmosis (RO), forward osmosis (FO)), and thermal-based (multistage flashing (MSF), multi-effect distillation (MED)) technologies are widely used

for obtaining freshwater; however, the high energy demand and variable feasibility hinder their implementation in poor countries [4,5]. For example, MSF is an energy-intensive technology and is a trade-off in various countries based upon their fuel resources. FO is still premature and cannot be used in the large-scale mass production of freshwater [6–8]. To tackle this issue and to envision a more sustainable future, efforts are being made to develop green and renewable technologies for obtaining freshwater that would satisfy the current needs, mainly in those countries. Various innovative technologies are being explored by researchers to meet this global challenge. These include graphene-based membranes [9], nanofiltration (NF) [10], nano adsorbent chillers [11], and solar-driven evaporation [12,13]. These emerging technologies are capable of converting waste heat into useful products in low-temperature conditions in remote sensing areas. Sztékler et al. [14] reported a silica gel-based three-bed sorption chiller for effective desalination in low-temperature conditions.

Solar-driven water evaporation has achieved tremendous interest owing to its excellent heat accumulation on the top surface with perfect thermal insulation towards downward heat flow. In solar stills, the poor optical concentration causes heat generation at the surface of the matrix while vapors are generated elsewhere in the system. This creates inevitable thermal leakage due to the wide gap between the heat and vapor generation points and ultimately results in lower evaporation [15–17]. To address these surface heat losses, the volumetric heating approach was implicated using nanofluids which shift the heat-generating point inside the fluid. Although this strategy has been implemented to some extent, it is inefficient for large-scale applications where high surface temperatures are required [18]. An interfacial evaporation strategy was proposed as a solution to sustain heat storage at the air–liquid interface and concurrently reduce heat losses due to radiation, conduction and convection with an output evaporation efficiency of up to ~90%, even under lower optical intensity conditions [19,20]. This approach relies on selective heating of the matrix where water entangles with the photothermal layer and evaporates immediately. This would avoid the volumetric heating which causes the solar-thermal conversion heat to disperse into the entire volume. The possibilities of harvesting sustainable solar energy make solar steam generation technology a promising path in the near future [21]. However, the practical applications of solar steam generating devices still suffer from poor thermal management, mechanical strength, thermal losses, and blockage of steam escape channels, which often occurs due to salt accumulation within the capillary channels for water supply, hence lowering the efficiency of solar-driven water yielding devices [22].

Numerous photothermal materials have been explored to harvest and convert the maximum solar flux into thermal energy. Fe<sub>2</sub>O<sub>3</sub> nanoparticles (NPs) have been reported to have excellent photothermal conversion [23], stability, and propensity for the removal of contaminants from water [24,25]. The valance band edge of Fe<sub>2</sub>O<sub>3</sub> is positive compared to the oxidation potential of water and it can be employed to achieve photocatalytic water oxidation reaction in the vicinity of sacrificial electron acceptors [26–28]. The proposed system in this study offers several advantages such as in situ conducting polymerization systems with  $\pi$ -conjugated electron systems [20] that have been recognized for having high absorption coefficients, smooth water transport channels, efficient thermal management, and good environmental stability. However, the fabrication and photothermal investigations of in situ polymerized Fe<sub>2</sub>O<sub>3</sub>@PPy-based nanocomposites have not been explored in the literature.

Herein, we demonstrate a solar-empowered interfacial thermal localization inspired Fe<sub>2</sub>O<sub>3</sub>@PPy/facial sponge solar evaporation structure (Fe<sub>2</sub>O<sub>3</sub>@PPy) which perfectly restricts the heat localization on the heating matrix and forbids downward heat flow. The pitch-black in situ polymerized Fe<sub>2</sub>O<sub>3</sub> photothermal layer enabled outstanding solar absorption (94%), excellent hydrophilicity, and sustainment under intense operating seawater circumstances (3.5 wt.%, no surface degradation/8.3 h continuous operation). An evaporation rate was recorded up to 1.52 kg m<sup>-2</sup> h<sup>-1</sup> under one sun solar intensity, whereas it is enhanced to 33.84 kg m<sup>-2</sup>/8.3 h under stimulated seawater conditions. The experiment yields an outstanding solar-thermal conversion efficiency potential of 95%, excluding

thermal losses. Besides, the Fe<sub>2</sub>O<sub>3</sub>@PPy solar evaporator sustained excellent surface temperature (41.9 °C) under 1 kW m<sup>-2</sup>. Raman spectroscopy revealed a complete rejection of methyl orange dye solution before and after desalination through a Fe<sub>2</sub>O<sub>3</sub>@PPy interfacial solar steam generator. Additionally, Inductively Coupled Plasma Atomic Emission Spectroscopy (ICP-AES) confirmed heavy metal rejection in condensed water which signifies that its NF potential meets the drinking water standard set by the World Health Organization (WHO). This technique lessens the utilization of Fe<sub>2</sub>O<sub>3</sub>@PPy as photothermal material while achieving high vapor flux. This offers an opportunity to expand the application of solar-thermal devices in compact, stand-alone, and portable systems.

## 2. Experimentation

### 2.1. Materials

All the required chemicals FeCl<sub>3</sub>·6H<sub>2</sub>O, NH<sub>4</sub>OH, and ethanol were acquired from Wuhan BASF Chemical Industries Co., Ltd., Wuhan, China, whereas pyrrole, phytic acid (PA, 50 wt.% in water), and buffered salts were purchased from Wuhan Guangfu fine synthetic industry, Wuhan, China. All the chemicals throughout the study were of standard analytical grade and were processed without further purification.

### 2.2. Preparation of Fe<sub>2</sub>O<sub>3</sub> Nanoparticles

Fe<sub>2</sub>O<sub>3</sub> NPs were synthesized by the well-known co-precipitation method. For this, iron oxide precursor FeCl<sub>3</sub>·6H<sub>2</sub>O (10. g) was dissolved evenly in deionized (DI) water (150 mL) using a magnetic stirrer at room temperature. Then, 2 mL ammonium hydroxide (NH<sub>4</sub>OH) solution was poured dropwise into the as-prepared solution at the rate of 1 mL min<sup>-1</sup> to initiate the precipitation. However, the pH was controlled during the whole synthesis and maintained up to 1. The following black suspension was stirred for 1 h at room temperature until the fine precipitates were obtained. Afterward, the followed suspension was stirred and heated at 80 °C for 2 h to yield a brown powder. The obtained brown powder was allowed to cool freely and was calcined at 500 °C for 4 h to achieve a pure crystalline hexagonal phase.

### 2.3. Deposition of Fe<sub>2</sub>O<sub>3</sub> NPs over the Facial Sponge

The prepared Fe<sub>2</sub>O<sub>3</sub> NPs were deposited over the circular-shaped facial sponge. Initially, the commercially available facial sponge was crafted into a circular shape with different diameters (3 to 4.5 cm). The Fe<sub>2</sub>O<sub>3</sub> NPs were immersed into a volatile terpeneol binder (C<sub>10</sub>H<sub>18</sub>O) using a mortar and pestle and a fine slurry was obtained. The slurry was coated evenly over the circular-shaped facial sponge using a BOSOBOP paintbrush. After deposition of Fe<sub>2</sub>O<sub>3</sub> NPs, it was preheated using a convection oven at 100 °C for 1 h to evaporate terpeneol binder, cooled down freely, and presented for the further in situ polymerization process.

### 2.4. Synthesis of Polypyrrole Monomers

In situ polymerization of conducting polypyrrole was carried out on Fe<sub>2</sub>O<sub>3</sub> NPs to enhance its omnidirectional solar absorption, NPs stability, and excellent wettability. For in situ polymerization of Fe<sub>2</sub>O<sub>3</sub> NPs coated facial sponge, 2.76 g of ammonium persulfate, (NH<sub>4</sub>)<sub>2</sub> S<sub>2</sub>O<sub>8</sub>, was thoroughly dissolved into deionized water (5 mL) and labeled as solution "A". Afterwards, 5 mL of the isopropanol alcohol (IPA) was taken into another beaker in which 0.86 mL pyrrole was poured along with 1.85 mL phytic acid (1:1 wt.% in water) while stirring continuously until the formation of a homogeneous mixture of dark brownish color which was labeled as solution "B". Subsequently, the "A" and "B" solutions were poured into spray bottles and sprayed on the Fe<sub>2</sub>O<sub>3</sub>-coated facial sponge according to an "A-B-A-B" sequence. The successive repetition of the spraying sequence was followed until the formation of a pitch dark, homogeneous coating of polypyrrole was accomplished on the Fe<sub>2</sub>O<sub>3</sub>/facial sponge surface, as illustrated in Figure 1. The deposited mass of polypyrrole

on the  $\text{Fe}_2\text{O}_3$ /facial sponge was calculated as 28 mg by estimating the comparative change in mass strategy. Detailed characterization is given in Supporting Information S1.

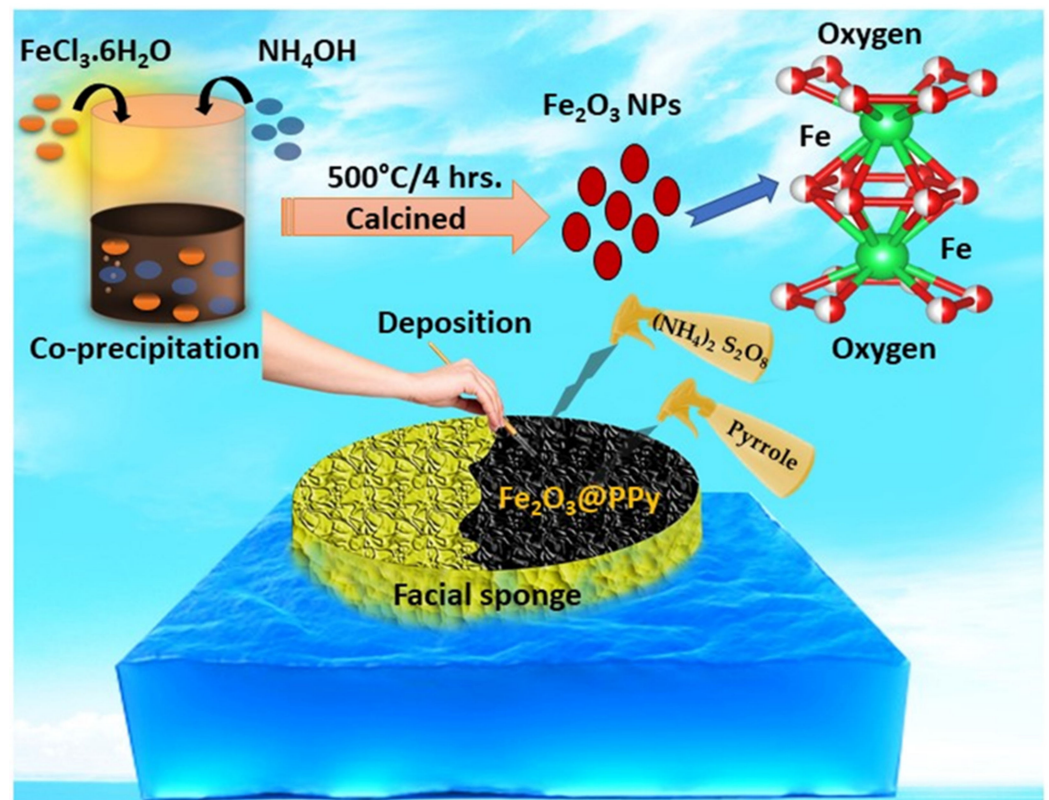


**Figure 1.** Schematic demonstration of the synthesis of  $\text{Fe}_2\text{O}_3$  NPs, deposition of  $\text{Fe}_2\text{O}_3$  NPs over the two-dimensional facial sponge, and its in situ polymerization of  $\text{Fe}_2\text{O}_3$ @PPy interfacial solar steam generator.

### 2.5. Solar to Vapor Conversion Efficiency ( $\eta$ )

The solar to vapor conversion efficiency ( $\eta$ ) of the  $\text{Fe}_2\text{O}_3$ @PPy evaporation system was calculated using Equations (1) and (2) [8,29]:

$$\eta = \dot{m}h_{LV}/q_i \quad (1)$$

$$h_{LV} = \lambda + C\Delta T \quad (2)$$

For the above equation,  $\dot{m}$  denotes the evaporation rate of the system when exposed to solar irradiation intensity subtracting the evaporation rate for bulk water (mass flux) and in the absence of light,  $h_{LV}$  denotes the phase change enthalpy from liquid-vapor along with sensible heat, and  $q_i$  is the irradiated solar intensity ( $1 \text{ kW m}^{-2}$ ).  $\lambda$  denotes the phase-changing latent heat ( $2430 \text{ kJ kg}^{-1}$  at  $30 \text{ }^\circ\text{C}$  and  $2256 \text{ kJ kg}^{-1}$  at  $100 \text{ }^\circ\text{C}$ ),  $C$  is the constant value which is  $4.2 \text{ kJ kg}^{-1} \text{ K}^{-1}$  (water-specific heat capacity), and  $\Delta T$  gives the elevation in the temperature of the water. The approximate ambient temperature ( $24.3 \text{ }^\circ\text{C}$ ) and humidity (43%) conditions were recorded.

### 2.6. Energy Balance (Heat Losses)

The energy balance equations for the  $\text{Fe}_2\text{O}_3$ @PPy solar evaporator were explained by thermal transport theory under one sun intensity ( $1 \text{ kW m}^{-2}$ ) [18,30]. The photothermal conversion efficiency of the  $\text{Fe}_2\text{O}_3$ @PPy solar evaporator was evaluated (Equations (3)–(5)) by assessing conductive heat losses via the following three phenomena: heat losses to bulk water via conduction ( $Q_{\text{Conduction}}$ ), convective heat losses to the surroundings ( $Q_{\text{Convection}}$ ), and radiative heat losses into the air ( $Q_{\text{Radiation}}$ ):

For conductive heat losses:

$$Q_{Conduction} = Ak \frac{(T_1 - T_2)}{\Delta l} \quad (3)$$

where  $A$  denotes the cross-section surface area of the device and  $k$  shows thermal conductivity to the bulk water ( $0.6 \text{ W m}^{-1} \text{ K}^{-1}$ ) [31]. The water temperature was recorded at two points via two embedded thermocouples separated by intermediate distance ( $\Delta l$ ).

For convective heat losses:

$$Q_{convection} = h (T_s - T_v) \quad (4)$$

where  $h$  is the convective heat transport coefficient (approximately  $10 \text{ W m}^{-2} \text{ K}^{-1}$ ),  $T_s$  is for the top surface temperature of solar-thermal conversion device, and  $T_v$  denotes the rise in the surrounding environmental temperature near the top surface due to the generation of hot vapors.

For radiative heat losses:

$$Q_{Radiation} = \varepsilon \sigma (T_s^4 - T_\infty^4) \quad (5)$$

where  $\varepsilon$  is the emission of the absorber ( $\sim 0.93$ ) [32],  $\sigma$  is the Stefan–Boltzmann constant ( $5.669 \times 10^{-8} \text{ W m}^{-2} \text{ K}^{-4}$ ), and  $T_\infty$  records the temperature of the adjacent surroundings. Upon the generation of hot vapors, the top surface which is covered by the vapors appears to be semitransparent to solar irradiation; as a result, heat loss can be determined by maximum and minimum values of radiative heat loss recorded as  $T_\infty = T_V$  (vapor temperature) and  $T_\infty = T_a$  (surrounding temperature), respectively.

### 2.7. Solar-Driven Steam Generation Setup

Solar-driven evaporation experiments were executed under a solar simulator (PLS-FX300HU) outputting the constant incident intensity at  $1 \text{ kW m}^{-2}$  (1 sun). A standard spectrum of 1.5 G AM was acquired by employing an optical filter. The self-floating and hydrophilic  $\text{Fe}_2\text{O}_3$ @PPy solar evaporation structure having 25 mm thickness was placed on the water surface filled in a petty dish (simulated seawater, heavy metal contaminated, and methyl orange solution) and was exposed under  $1 \text{ kW m}^{-2}$  solar intensity. An advanced electronic balance (Mettler Toledo, ME204) up to 0.001 g resolution was utilized to calculate the time-dependent mass change variation. After the stabilization of the whole evaporation system, all the evaporation rates were measured under one solar intensity. Moreover, the ionic concentrations of salt and heavy metal ions were recorded by using an inductively coupled plasma-optical emission spectrometry (ICP-AES, E.P. Optimal 8000) before and after treating the water. All the experimental measurements were done at ambient environmental conditions, at closest mean values  $\sim 24.3 \text{ }^\circ\text{C}$  temperature and  $\sim 43\%$  humidity. Surface temperatures were recorded by employing the Hand-Held Optical Meter Model.

## 3. Results and Discussion

### 3.1. Chemical States and Crystal Structure

Hematite ( $\text{Fe}_2\text{O}_3$ ) is the most attractive and significant metal oxide due to well-visible light absorption, solar energy conversion, environmental compatibility, and excellent chemical stability under intense conditions. It has been used widely for wastewater treatment and photocatalytic applications [33]. Figure 2a presents the structural configuration of the hematite crystalline hexagonal structure. It is an n-type semiconductor that occupies the largest fraction of visible light, the valance band of hematite consists of O  $2p$  and Fe  $3d$  orbitals, constituting a complex structure, and the conduction band consists of  $3d$  orbitals of Fe [33]. Figure 2b shows the X-ray diffraction spectra of  $\text{Fe}_2\text{O}_3$  nanoparticles. The XRD patterns of  $\text{Fe}_2\text{O}_3$  nanoparticles match perfectly with the standard data (JCPDS 33-0664). The crystal structure analysis shows the hexagonal structure with peaks appearing at  $2\theta$  values of  $25^\circ$ ,  $34^\circ$ ,  $36^\circ$ ,  $42^\circ$ ,  $48^\circ$ ,  $54.5^\circ$ ,  $57.6^\circ$ ,  $62.5^\circ$ , and  $64.1^\circ$  correspond to the (0 1 2),

(1 1 0), (1 1 3), (2 0 2), (0 2 4), (1 1 6), (0 1 8), (2 1 4), and (3 0 0) planes of the  $\text{Fe}_2\text{O}_3$  nanoparticles, respectively. No extra peaks appeared in a given pattern, showing its hydroxides transformation to hematite during the coprecipitation process [25].

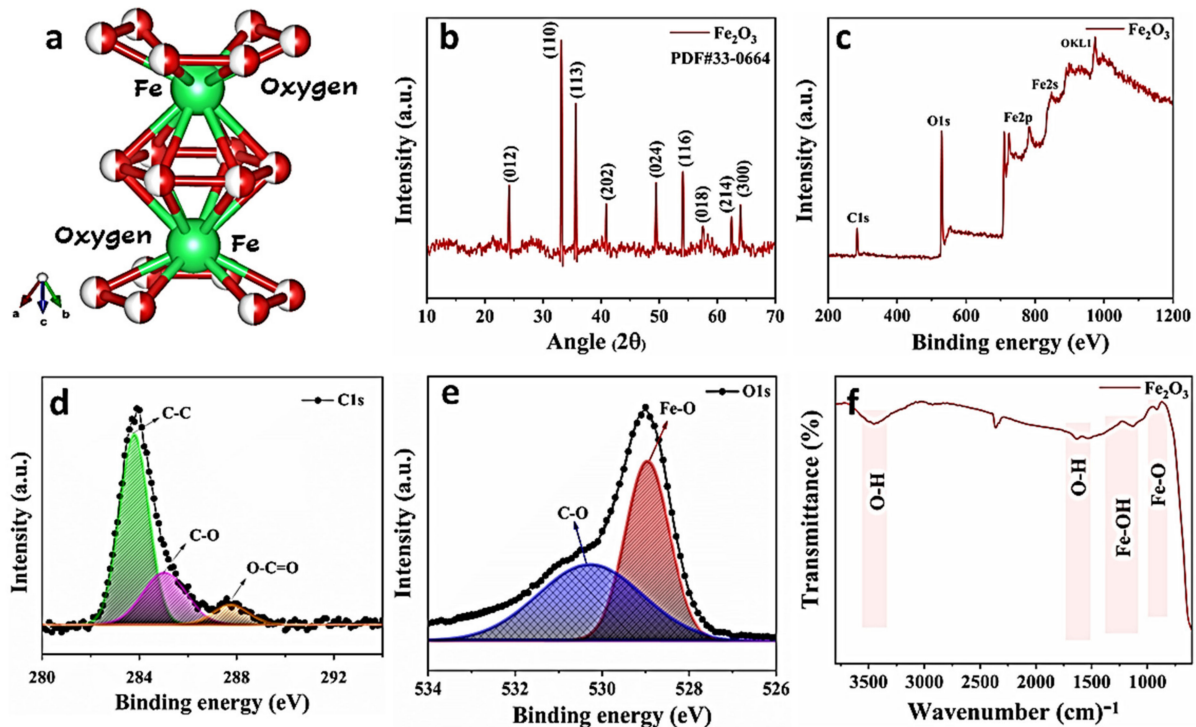


**Figure 2.** (a–f) Crystal structure and chemical states as-synthesized  $\text{Fe}_2\text{O}_3$  nanoparticles (NPs); (a) crystallographic unit cell of  $\text{Fe}_2\text{O}_3$ ; (b) XRD spectra of  $\text{Fe}_2\text{O}_3$  NPs; (c) XPS survey of  $\text{Fe}_2\text{O}_3$  NPs; (d) C 1s spectrum; (e) O 1s spectra of  $\text{Fe}_2\text{O}_3$  NPs; (f) FTIR stretching bonds peaks of  $\text{Fe}_2\text{O}_3$  NPs.

The XPS survey spectrum was analyzed to study the elemental electronic states present on the surface of  $\text{Fe}_2\text{O}_3$  nanoparticles. The homogeneous elemental distribution impacts the oxidation states shifting which could optimize the material's optical, thermal, and magnetic properties. The XPS survey spectrum of  $\text{Fe}_2\text{O}_3$  shows the presence of Fe, O, and C on the sample surface as shown in Figure 2c. The prominent peak appears at 534.44 eV which attributes to the  $1s \text{ O}^{-2}$  ions through which the highest range at 710.55 eV corresponds to Fe 2p ions. The deconvolution of the peaks for each element was done by applying Gaussian fit to observe the changes in the homogeneous ion distribution in the  $\text{Fe}_2\text{O}_3$  lattice. Figure S1 shows the Fe 2p spectra with ionic states  $\text{Fe } 2p_{1/2}$  and  $\text{Fe } 2p_{3/2}$  corresponding to 714.15 and 728.55 eV binding energies, respectively. Figure 2d shows the C 1s spectra which have three prominent peaks at binding energies 283, 284.5, and 288 eV, which correlate to C-C, C-O, and O-C=O bonding, respectively. The characteristic bands appearing at 532 and 529 eV are attributed to the O 1s XPS spectra which correspond to the C-O and Fe-O bonding (Figure 2e). The physicochemical characteristics of the prepared  $\text{Fe}_2\text{O}_3$  NPs were investigated through the FTIR spectrum, as shown in Figure 2f. The absorption peaks appearing at 1000 and 1300  $\text{cm}^{-1}$  correspond to the Fe-O and Fe-OH stretching vibrations, respectively. Besides, the absorption band appearing at 1600 and 3500  $\text{cm}^{-1}$  are referred to as the presence of hydroxyl group –OH.

### 3.2. Fabrication of $\text{Fe}_2\text{O}_3$ @PPy Solar Evaporator

Figure 3a presents the digital image of the step-by-step preparation of the  $\text{Fe}_2\text{O}_3$ @PPy-based solar evaporation device. Initially, the super hydrophilic and mechanically robust pristine facial sponge was chosen as substrate and carved carefully in a circular shape with the dimensions of 2 cm × 2 cm × 1 cm = 4  $\text{cm}^3$ , incorporated by vertically oriented

water channels for water transport. This facial sponge has several advantages when compared to commercial polyurethane (PU) foam including flexibility, self-floating ability, and remarkable heat-insulating capability [34]. The obtained reddish-orange color gel was deposited uniformly on a super hydrophilic circular-shaped facial sponge using a BOSOBO paintbrush. Polypyrrole is an organic polymer produced by the oxidative polymerization of pyrrole. It is an intrinsically conducting polymer and has a heterocyclic structure with the formula  $H(C_4H_2NH)_nH$ . The surface of polypyrrole films presents fractal properties allowing ionic diffusion with anomalous diffusion patterns [35]. Indeed, polypyrrole coating offers good absorbing capacity, mechanical robustness, biocompatibility, and long-term cytotoxicity [36].

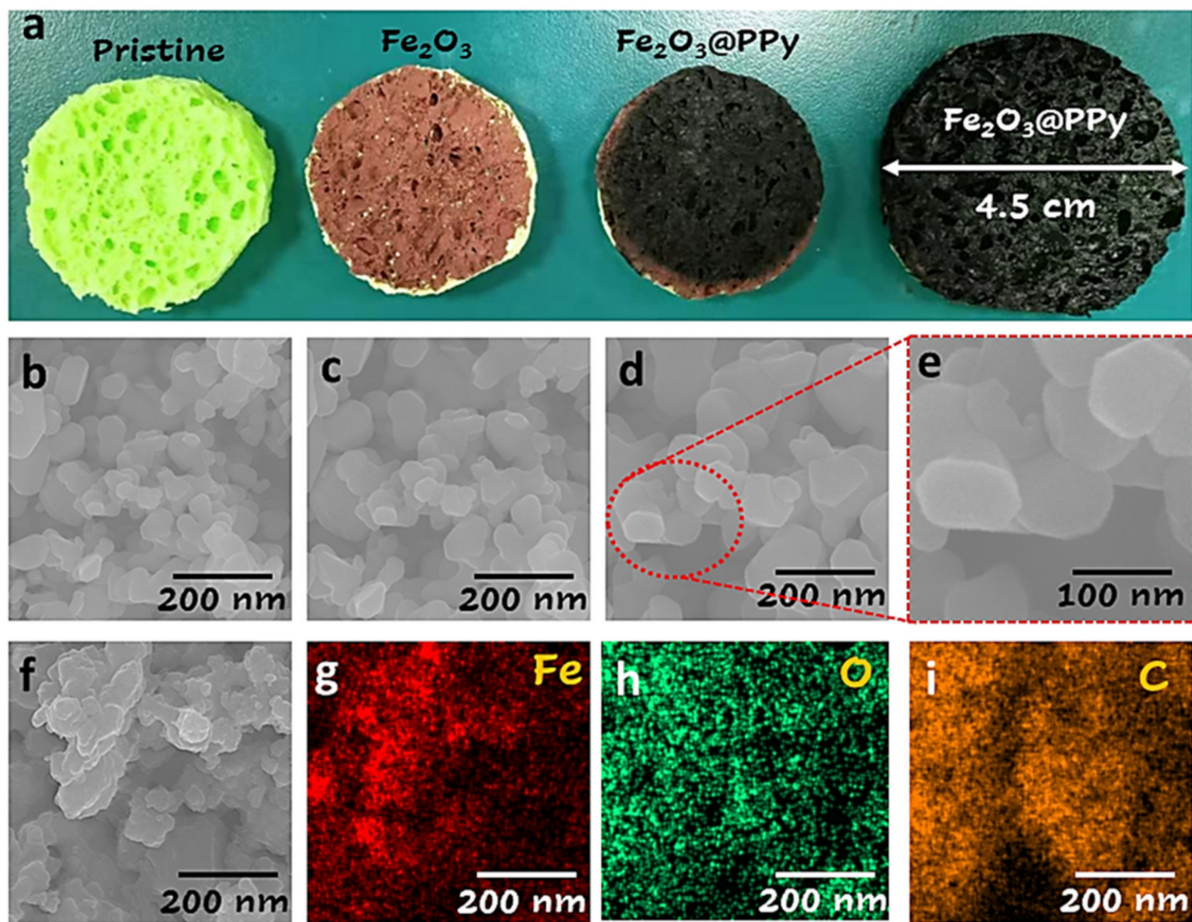


**Figure 3.** (a) Photograph of the step-by-step preparation of Fe<sub>2</sub>O<sub>3</sub>@PPy solar evaporator with various sizes. (b–f) Fe<sub>2</sub>O<sub>3</sub> nanoparticles under different resolutions. (f–i) EDS mapping of Fe<sub>2</sub>O<sub>3</sub> nanoparticles.

To increase the dispersion and distribution of incident solar radiation (lowering the refractive index) and solar absorbing capacity, a highly conductive polypyrrole polymer was coated on the Fe<sub>2</sub>O<sub>3</sub> surface by following a facile in situ polymerization. For this, the composing of the two monomer solutions is accomplished (as explained above in Section 2.3) and sequentially sprayed on the surface of the Fe<sub>2</sub>O<sub>3</sub>/facial sponge until the reddish-orange surface is turned into a pitch dark color. The digital photograph of the Fe<sub>2</sub>O<sub>3</sub>@PPy prototype in a different size is presented in Figure 3a. Figure 3b–d demonstrates the FESEM images of Fe<sub>2</sub>O<sub>3</sub> NPs, showing the uniform morphology of the prepared Fe<sub>2</sub>O<sub>3</sub> NPs with an average size of 40 nm, thus having a high surface-to-volume ratio for enhanced photothermal conversion activity. Fe<sub>2</sub>O<sub>3</sub> NPs EDS analysis confirms the presence of Fe (45%), O (45%), and C (10%) as shown in Figure 3f–i, respectively.

### 3.3. Superhydrophilic Evaporation Channels

Super hydrophilic solar-driven interfacial evaporation systems with an inter-linked porous structure enhance solar to vapor conversion efficiency due to surface roughness with optimized defect chemistry, which ultimately increases the absorption capacity and diffuse reflection [37,38]. Figure 4a,b demonstrates the FESEM images of cross-linked open porous morphology of super hydrophilic facial sponge with a uniform porous structure having plenty of micrometer-sized open-pore channels. The vertical cross-linked water channels occupied by open pores reveal the great potential for capillary pumping of water and a high evaporation rate at the water surface. Figure 4c,d reveals the morphological analysis of the surface configuration of the polymerized  $\text{Fe}_2\text{O}_3@\text{PPy}$  interfacial heating device, showing an inset of complex surface structure where the built-in cross-linked facial sponge surface is coated with a pitch dark color layer of  $\text{Fe}_2\text{O}_3@\text{PPy}$  NPs. The  $\text{Fe}_2\text{O}_3@\text{PPy}$  NPs are uniformly distributed over the surface with no structural alteration, exhibiting an overall condensed texture due to successive polymerizations. The complex surface structure induces multiple rays within the matrix, enabling omnidirectional absorption while offering a large surface area for heat distribution. This would ultimately enhance the light absorption ability of the device while restricting the downward thermal conduction to achieve a high evaporation surface temperature [39]. The in situ polymerization plays a decisive role in the defect chemistry with enhanced solar absorption, wettability, and tortuosity of the device [35,39]. The observed surface configuration and device morphology owe excellent capability for outstanding heat accumulations, smooth water transportation, and prevention of downward thermal conduction to avoid heat losses.

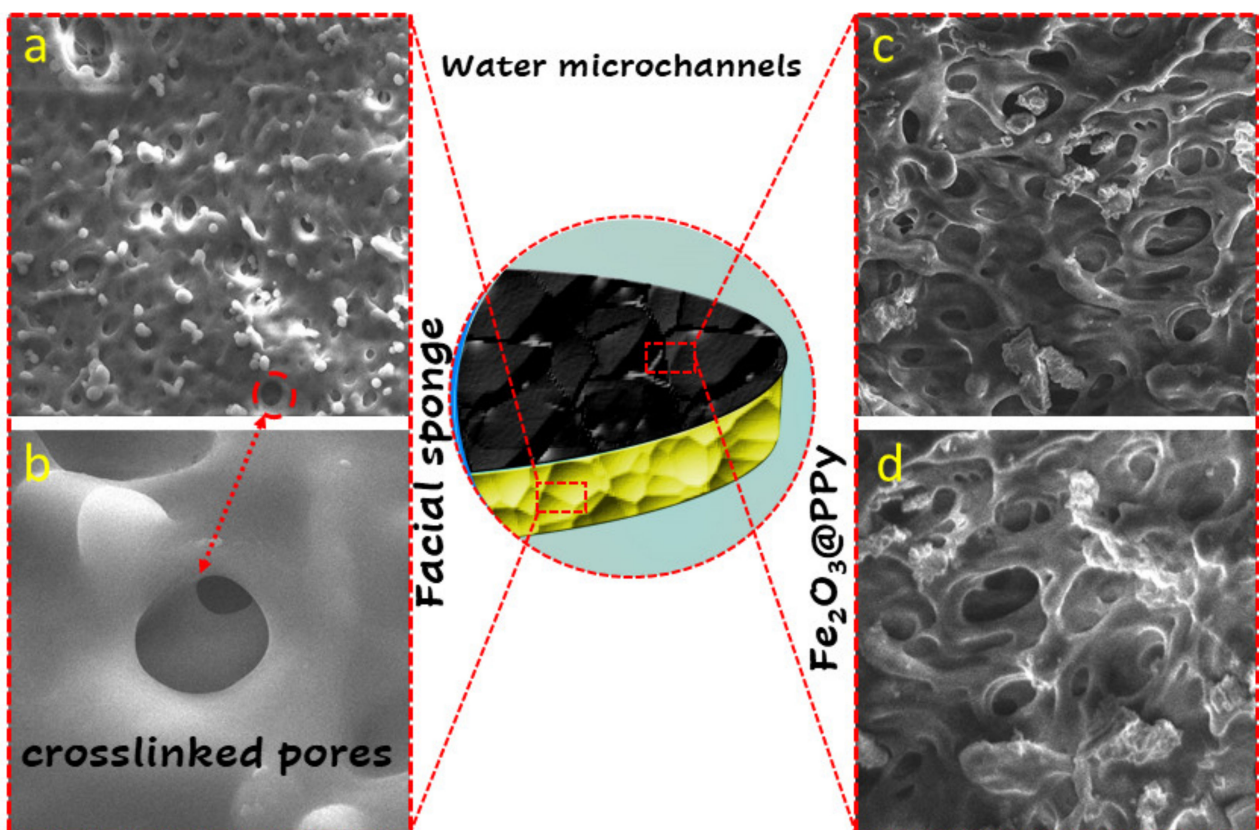


**Figure 4.** Super hydrophilic and crosslinked water evaporation channels. (a,b) FESEM image of the crosslinked open porous structure of super hydrophilic facial sponge. (c,d) FESEM image of in-situ polymerized  $\text{Fe}_2\text{O}_3$ /facial sponge showing rugged surface texture with intensified pitch-black color with interlinked vertical channels.

### 3.4. Fe<sub>2</sub>O<sub>3</sub>@PPy Solar Evaporator

The interfacial evaporation devices for seawater desalination reveal the great potential for the maximum utilization of solar energy and controlling energy losses [40]. Figure 5a shows the energy balance for the interfacial Fe<sub>2</sub>O<sub>3</sub>@PPy solar evaporator based on interfacial heating which exhibits negligible heat losses under solar irradiation. It also accompanies the simultaneous liquid to vapor phase transition by sustainment of heat at the air–liquid interface. The ultra-black composite surface effectively harvests the incident light energy for multiple diffuse reflections which optimize the incident light energy and control light losses.

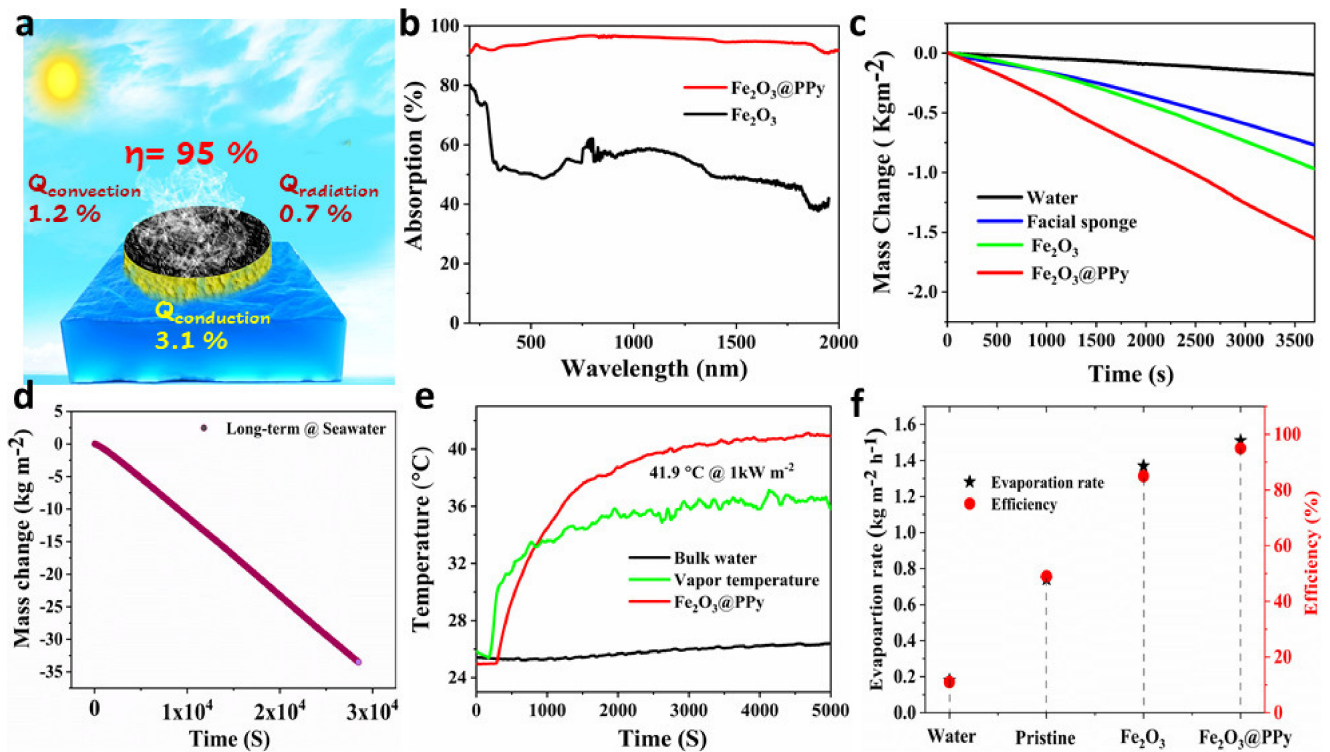


**Figure 5.** (a) Energy balance diagram of Fe<sub>2</sub>O<sub>3</sub>@PPy solar evaporator with conductive, convective, and radiative losses. (b) Full range of the UV-Vis absorption spectrum of Fe<sub>2</sub>O<sub>3</sub> and Fe<sub>2</sub>O<sub>3</sub>@PPy solar evaporator. (c) Mass change in water, facial sponge, Fe<sub>2</sub>O<sub>3</sub>/facial sponge, and Fe<sub>2</sub>O<sub>3</sub>@PPy solar evaporators under one sun illumination. (d) The long-term evaporation performance with minor disparity under one sun irradiation for continuous evaporation up to 8.3 h in seawater conditions. (e) Surface temperatures of Fe<sub>2</sub>O<sub>3</sub>@PPy solar evaporator and vapors. (f) The achieved evaporation rates and respective solar to vapor conversion efficiencies of the designed four evaporation systems.

The incoming solar energy is typically divided into two components, solar to vapor efficiency and undesired heat losses. The overall efficiency of the interfacial Fe<sub>2</sub>O<sub>3</sub>@PPy solar evaporator was evaluated (95%) excluding the heat losses to the environment, e.g., thermal loss via conduction to underlying water (3.1%), heat transfer via convection through vapors (1.2%), and thermal loss to the adjacent environment via radiation (0.7%). The optical absorptions of the Fe<sub>2</sub>O<sub>3</sub> and Fe<sub>2</sub>O<sub>3</sub>@PPy solar evaporator were analyzed by UV-Vis spectroscopy over the whole solar spectrum (200–2500 nm). The UV-Vis absorption spectrum of pure Fe<sub>2</sub>O<sub>3</sub> and in situ polymerized Fe<sub>2</sub>O<sub>3</sub>@PPy solar evaporator are demonstrated in Figure 5b. An outstanding solar absorption (94%) potential is exhibited by the in situ polymerized Fe<sub>2</sub>O<sub>3</sub>@PPy interfacial solar evaporator and is significantly enhanced compared to the simple Fe<sub>2</sub>O<sub>3</sub> NPs with negligible transmission (4%) and reflection (2%) calculated by the following absorption formula: (1-T-R).

The supreme solar-harvesting potential can be featured in the crimped structural configuration of in situ polymerizations of Fe<sub>2</sub>O<sub>3</sub> NPs which can efficiently sustain and

localize the heat by intrinsically dispensing the incoming solar radiations on the composite surface, which sculpts the basic mechanism of the interfacial solar evaporating structure [41]. Herein, we demonstrate a comparative analysis of four systems for the interfacial solar evaporation phenomena, including pure water, super hydrophilic facial sponge, Fe<sub>2</sub>O<sub>3</sub>/facial sponge, and Fe<sub>2</sub>O<sub>3</sub>@PPy solar evaporator. Each of the evaporation systems was exposed under simulated one solar irradiation (1 kW m<sup>-2</sup>) and time-dependent mass change was recorded via a weighing balance with 0.0001 g resolution for one hour. An enhancement in thermal localization over the top surface escalates the vapor generation; thus, the Fe<sub>2</sub>O<sub>3</sub>@PPy solar steam generator shows the outstanding mass variations (1.52 kg m<sup>-2</sup>) comparative to the bulk water and other evaporation systems, as shown in Figure 5c. Furthermore, mass change for Fe<sub>2</sub>O<sub>3</sub>@PPy solar evaporator for multiple solar intensities was recorded, as provided in Figure S2. Although there are some solar steam generation devices reported for good evaporation rate, the major challenge being faced by these devices is the deformation of structural configuration with mechanical frailty mainly due to salt accumulation and surface distortion by the deposition of organic and inorganic impurities present in seawater, which leads to the compositional disintegration after operating a few cycles and lower efficiency of the device [5,12]. To address this, the evaporating device was operated for continuous operation for long-term performance to inspect the mechanical strength and persistence in evaporation efficiency, which reveals that Fe<sub>2</sub>O<sub>3</sub>@PPy remarkably achieved the consistency in steam generation under simulated seawater for continuous 8.3 h (33.84 kg m<sup>-2</sup>) with the minimal disparity in the evaporation rate under 1 kWm<sup>-2</sup>, showing excellent scalability for operating over a long time period (Figure 5d). The comparative analysis of temperature gradient for the bulk water, vapor temperature, and Fe<sub>2</sub>O<sub>3</sub>@PPy solar evaporating device under one solar intensity (1 kW m<sup>-2</sup>) is illustrated in Figure 5e. The surface temperature achieved a maximum value up to 41.9 °C under one sun illumination by a Fe<sub>2</sub>O<sub>3</sub>@PPy solar evaporator that is comparatively more efficient than other solar-thermal conversion devices. This is attributed to the remarkable heat localization on the photothermal layer and excellent insulation from downward heat conduction which ultimately leads to achieving higher evaporation efficiency. Figure 5f demonstrates the analysis of the comparative evaporation rate for the four developed systems, which reveals that the evaporation rate of the Fe<sub>2</sub>O<sub>3</sub>@PPy solar evaporator (1.52 kg m<sup>-2</sup> h<sup>-1</sup>) and photothermal conversion efficiency (95%) are notably higher comparative to the simple Fe<sub>2</sub>O<sub>3</sub>/facial sponge and many other evaporation systems to date [42–44]. However, a detailed solar evaporation efficiencies-based comparison is provided in Supplementary Materials Table S1.

### 3.5. Self-Rejection Potential

The self-floatable Fe<sub>2</sub>O<sub>3</sub>@PPy solar evaporator absorbs the entire solar spectrum and is transformed into confined thermal packs for efficient vapor generation which can be condensed to pure freshwater by completely rejecting heavy metal ions, primary salt ions, and wastewater contamination. Stimulated seawater and heavy metal ions, as well as methyl orange dye solutions were prepared to verify the self-rejection potential of the Fe<sub>2</sub>O<sub>3</sub>@PPy solar evaporator. More importantly, Raman spectroscopy analysis of methyl orange dye solution was carried out before evaporation and in condensed water. Figure 6a,b represent the microscopical image of the methyl orange dissolved water solution, and the condensed water exhibiting the complete removal of methyl orange and pure water droplets could be seen clearly. Figure 6c represents the Raman spectra of methyl orange dissolved water solution and condensed water after treating through interfacial Fe<sub>2</sub>O<sub>3</sub>@PPy solar evaporator. The methyl orange dissolved solutions show the methyl orange band appearing at 1500 and 1600 cm<sup>-1</sup>, exhibiting the presence of methyl orange, and condensed water shows a smooth spectrum with no bands appearing in the range of 1400 to 1600 cm<sup>-1</sup>, which reveals the complete removal of methyl orange after evaporation through the interfacial Fe<sub>2</sub>O<sub>3</sub>@PPy solar evaporator.

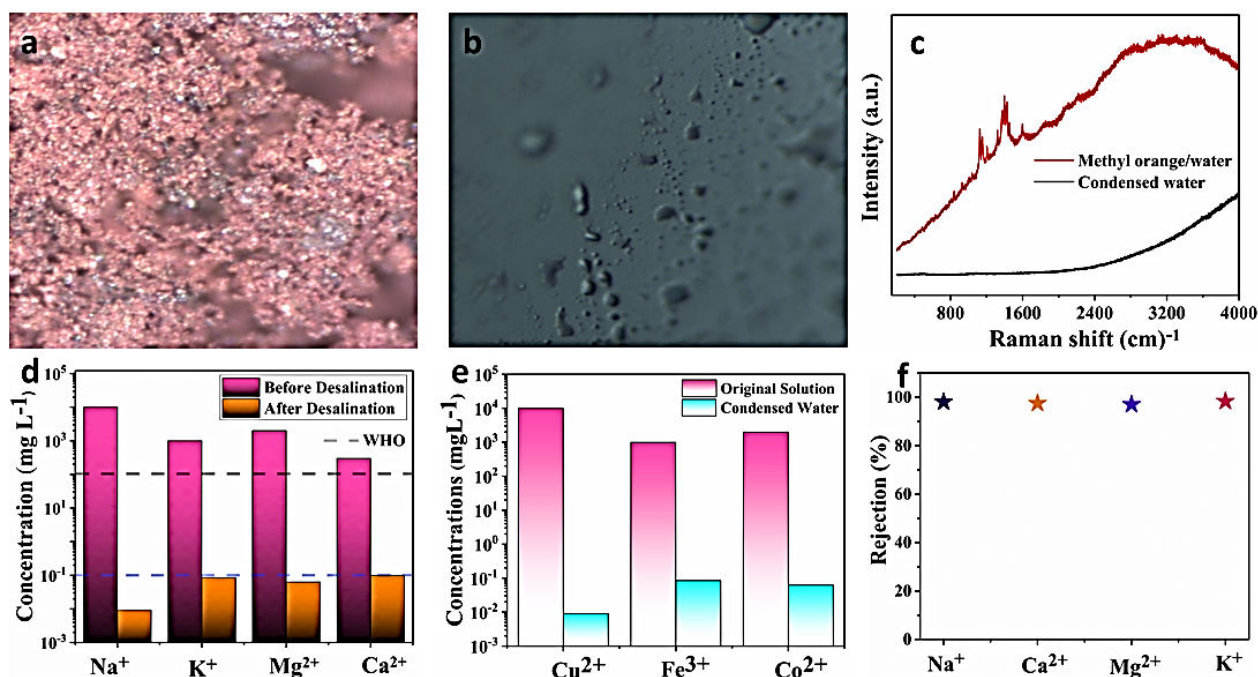


**Figure 6.** (a,b) Microscopical image of methyl orange/water solution and condensed water after evaporation through Fe<sub>2</sub>O<sub>3</sub>@PPy solar evaporator during Raman spectroscopy. (c) Raman spectra of methyl-orange dissolved water and condensed water show no peaks that show excellent degradation. (d,e) Concentration of the primary metals ions, and heavy metals ions before and after desalination. (f) Complete rejection of primary salt ions in stimulated seawater.

The Fe<sub>2</sub>O<sub>3</sub>@PPy solar evaporator encompasses the excellent self-resistant capability against the salt and heavy metal ions within the vertically oriented cross-linked macro water channels of super hydrophilic facial sponge and ensures the standard of purity level of freshwater yield. As the cross-linked water transportation network promotes water evaporation only through the molecular mode, it also assists in water purification against the removal of primary metal ions and heavy metal ions. ICP-AES was employed to assess the soluble salt ions concentration gradient (3.5 wt.% NaCl, CaCl<sub>2</sub>, KCl, MgSO<sub>4</sub>), and the desalination potential of the Fe<sub>2</sub>O<sub>3</sub>@PPy solar evaporator was measured through simulated and condensed water. The result obtained from ICP-AES exhibits an appreciable decrease in the ionic concentrations of Na<sup>+</sup>, K<sup>+</sup>, Ca<sup>2+</sup>, and Mg<sup>2+</sup> in the collected water comparative to the initial concentration in the simulated seawater. The result is far below the standards of drinking water set by the WHO [29,45], thus fetching the application of Fe<sub>2</sub>O<sub>3</sub>@PPy solar evaporator up to standard drinking water as illustrated in Figure 6d. Furthermore, the commercial waste contains high concentrations of heavy metal ions which are hazardous and predominately contaminate the water [46,47]. The condensed water was also examined for the engrossment of intruded heavy metals ions, e.g., Cu<sup>2+</sup>, Fe<sup>3+</sup>, and Co<sup>2+</sup>; the concentration level of these heavy metal ions was significantly lessened from 1000 mg L<sup>-1</sup> to 0.0084, 0.0065, and 0.0032 mg L<sup>-1</sup> after evaporation via the Fe<sub>2</sub>O<sub>3</sub>@PPy solar evaporator as shown in Figure 6e. The self-resistant potential of the interfacial Fe<sub>2</sub>O<sub>3</sub>@PPy solar evaporator against rejection of primary metals ion and heavy metal ions of simulated seawater to purify the water meets 100% of the standards for drinking water level as demonstrated in Figure 6f, proving the outstanding potential for treating sewage water for freshwater production.

#### 4. Conclusions

In summary, a self-floating and flexible in situ polymerized Fe<sub>2</sub>O<sub>3</sub>@PPy solar evaporator was composed of a super hydrophilic facial sponge with vertically cross-linked water channels as a solar-driven interfacial evaporating system for intensified heat accumulation and enhanced solar-thermal conversion efficiency. The pitch-dark rough surface texture of

the photothermal layer induces multiple rays within the heating matrix, which facilitates the omnidirectional solar absorption and offers defect abundant surface to promote heat localization and achieve high surface temperature (41.9 °C) along with high evaporation efficiency (90% excluding heat losses). The self-dissolving potential against methyl-orange and multimedia rejection exhibit an excellent functioning capability and self-regenerating potential against various impurities while maintaining the structural configuration without any deformation or antifouling nature. The presented work paves the way for new prospects for engineering a low cost, highly efficient with excellent heat localization, scalable, easily manufactured, and industrially compatible interfacial solar evaporator with commercially available precursors having excellent potential against the rejection of various impurities. Moreover, future work on the determination of mechanical resistance of the system with regards to relatively prolonged operating cycles can help to quantify the operational cost and maintenance cost of the system. It also makes our device a promising solution for implementing at an industrial scale in remote locations to cope with water scarcity issues.

**Supplementary Materials:** The following are available online at <https://www.mdpi.com/article/10.3390/cryst11121509/s1>, Note S1: Characterization; Figure S1. Fe 2p scan of Fe<sub>2</sub>O<sub>3</sub> NPs; Figure S2. Time dependent mass change under different solar intensities; Table S1. Detailed performance comparison with the recent successful solar evaporators.

**Author Contributions:** Conceptualization, N.A. and M.S.I.; methodology, Y.L. and I.A.; software, L.A.A. and M.N.; validation, S.A., I.A. and Y.L.; formal analysis, M.Y. and L.A.A.; investigation, M.S.I., I.A. and Y.L.; resources, S.A. and A.E.S.; data curation, S.A. and A.E.S.; writing—original draft preparation, Y.L. and N.A.; writing—review and editing, M.S.I. and I.A.; visualization, L.A.A., M.N. and M.Y.; supervision, I.A.; project administration, M.S.I., I.A. and Y.L.; funding acquisition, S.A. and A.E.S. All authors have read and agreed to the published version of the manuscript.

**Funding:** The APC was funded by Researchers Supporting Project number (RSP-2021/387), King Saud University, Riyadh, Saudi Arabia.

**Institutional Review Board Statement:** Not applicable.

**Informed Consent Statement:** Not applicable.

**Acknowledgments:** The authors extend their appreciation to King Saud University for funding this work through Researchers Supporting Project number (RSP-2021/387), King Saud University, Riyadh, Saudi Arabia.

**Conflicts of Interest:** The authors declare that they have no known competing financial interests or personal relationships that could have appeared to influence the work reported in this paper.

## References

1. Wu, X.; Wu, Z.; Wang, Y.; Gao, T.; Li, Q.; Xu, H. All-Cold Evaporation under One Sun with Zero Energy Loss by Using a Heatsink Inspired Solar Evaporator. *Adv. Sci.* **2021**, *8*, 2002501. [[CrossRef](#)] [[PubMed](#)]
2. Wang, S.; Fan, Y.; Wang, F.; Su, Y.; Zhou, X.; Zhu, Z.; Sun, H.; Liang, W.; Li, A. Potentially scalable fabrication of salt-rejection evaporator based on electrogenerated polypyrrole-coated nickel foam for efficient solar steam generation. *Desalination* **2021**, *505*, 114982. [[CrossRef](#)]
3. Tao, P.; Ni, G.; Song, C.; Shang, W.; Wu, J.; Zhu, J.; Chen, G.; Deng, T. Solar-driven interfacial evaporation. *Nat. Energy* **2018**, *3*, 1031–1041. [[CrossRef](#)]
4. Awasthi, A.; Kumari, K.; Panchal, H.; Sathyamurthy, R. Passive solar still: Recent advancements in design and related performance. *Environ. Technol. Rev.* **2018**, *7*, 235–261. [[CrossRef](#)]
5. Wang, P. Emerging investigator series: The rise of nano-enabled photothermal materials for water evaporation and clean water production by sunlight. *Environ. Sci. Nano* **2018**, *5*, 1078–1089. [[CrossRef](#)]
6. Liu, X.; Mishra, D.D.; Wang, X.; Peng, H.; Hu, C. Towards highly efficient solar-driven interfacial evaporation for desalination. *J. Mater. Chem. A* **2020**, *8*, 17907–17937. [[CrossRef](#)]
7. Shi, Y.; Zhang, C.; Li, R.; Zhuo, S.; Jin, Y.; Shi, L.; Hong, S.; Chang, J.; Ong, C.; Wang, P. Solar evaporator with controlled salt precipitation for zero liquid discharge desalination. *Environ. Sci. Technol.* **2018**, *52*, 11822–11830. [[CrossRef](#)]
8. Xu, J.; Wang, Z.; Chang, C.; Fu, B.; Tao, P.; Song, C.; Shang, W.; Deng, T. Solar-driven interfacial desalination for simultaneous freshwater and salt generation. *Desalination* **2020**, *484*, 114423. [[CrossRef](#)]

9. Homaeigohar, S.; Elbahri, M. Graphene membranes for water desalination. *NPG Asia Mater.* **2017**, *9*, e427. [[CrossRef](#)]
10. Dayarathne, H.N.P.; Choi, J.; Jang, A. Enhancement of cleaning-in-place (CIP) of a reverse osmosis desalination process with air micro-nano bubbles. *Desalination* **2017**, *422*, 1–4. [[CrossRef](#)]
11. Sztékler, K.; Kalawa, W.; Nowak, W.; Mika, Ł.; Krzywański, J.; Grabowska, K.; Sosnowski, M.; Alharbi, A.A. Performance Evaluation of a Single-Stage Two-Bed Adsorption Chiller with Desalination Function. *J. Energy Resour. Technol.* **2020**, *143*, 082101. [[CrossRef](#)]
12. Irshad, M.S.; Arshad, N.; Wang, X. Nanoenabled Photothermal Materials for Clean Water Production. *Glob. Chall.* **2021**, *5*, 2000055. [[CrossRef](#)]
13. Fuzil, N.S.; Othman, N.H.; Alias, N.H.; Marpani, F.; Othman, M.H.D.; Ismail, A.F.; Lau, W.J.; Li, K.; Kusworo, T.D.; Ichinose, I.; et al. A review on photothermal material and its usage in the development of photothermal membrane for sustainable clean water production. *Desalination* **2021**, *517*, 115259. [[CrossRef](#)]
14. Sztékler, K.; Kalawa, W.; Nowak, W.; Mika, L.; Gradziel, S.; Krzywanski, J.; Radomska, E. Experimental Study of Three-Bed Adsorption Chiller with Desalination Function. *Energies* **2020**, *13*, 5827. [[CrossRef](#)]
15. Ito, Y.; Tanabe, Y.; Han, J.; Fujita, T.; Tanigaki, K.; Chen, M. Multifunctional porous graphene for high-efficiency steam generation by heat localization. *Adv. Mater.* **2015**, *27*, 4302–4307. [[CrossRef](#)]
16. He, S.; Chen, C.; Kuang, Y.; Mi, R.; Liu, Y.; Pei, Y.; Kong, W.; Gan, W.; Xie, H.; Hitz, E.; et al. Nature-inspired salt resistant bimodal porous solar evaporator for efficient and stable water desalination. *Energy Environ. Sci.* **2019**, *12*, 1558–1567. [[CrossRef](#)]
17. Irshad, M.S.; Wang, X.; Abbas, A.; Yu, F.; Li, J.; Wang, J.; Mei, T.; Qian, J.; Wu, S.; Javed, M.Q. Salt-resistant carbon dots modified solar steam system enhanced by chemical advection. *Carbon* **2021**, *176*, 313–326. [[CrossRef](#)]
18. Ghasemi, H.; Ni, G.; Marconnet, A.M.; Loomis, J.; Yerci, S.; Miljkovic, N.; Chen, G. Solar steam generation by heat localization. *Nat. Commun.* **2014**, *5*, 4449. [[CrossRef](#)]
19. Yin, H.; Xie, H.; Liu, J.; Zou, X.; Liu, J. Graphene tube shaped photothermal layer for efficient solar-driven interfacial evaporation. *Desalination* **2021**, *511*, 115116. [[CrossRef](#)]
20. Irshad, M.S.; Wang, X.; Abbasi, M.S.; Arshad, N.; Chen, Z.; Guo, Z.; Yu, L.; Qian, J.; You, J.; Mei, T. Semiconductive, Flexible MnO<sub>2</sub> NWs/Chitosan Hydrogels for Efficient Solar Steam Generation. *ACS Sustain. Chem. Eng.* **2021**, *9*, 3887–3900. [[CrossRef](#)]
21. Liu, J.; Zou, X.; Cai, Z.; Peng, Z.; Xu, Y. Polymer based phase change material for photo-thermal utilization. *Sol. Energy Mater. Sol. Cells* **2021**, *220*, 110852. [[CrossRef](#)]
22. Li, X.; Cooper, T.; Xie, W.; Hsu, P.-C. Design and Utilization of Infrared Light for Interfacial Solar Water Purification. *ACS Energy Lett.* **2021**, *6*, 2645–2657. [[CrossRef](#)]
23. Larsen, G.K.; Farr, W.; Hunyadi Murph, S.E. Multifunctional Fe<sub>2</sub>O<sub>3</sub>–Au Nanoparticles with Different Shapes: Enhanced Catalysis, Photothermal Effects, and Magnetic Recyclability. *J. Phys. Chem. C* **2016**, *120*, 15162–15172. [[CrossRef](#)]
24. Mansourpanah, Y.; Rahimpour, A.; Tabatabaei, M.; Bennett, L. Self-antifouling properties of magnetic Fe<sub>2</sub>O<sub>3</sub>/SiO<sub>2</sub>-modified poly (piperazine amide) active layer for desalting of water: Characterization and performance. *Desalination* **2017**, *419*, 79–87. [[CrossRef](#)]
25. Gopal, R.A.; Song, M.; Yang, D.; Lkhagvaa, T.; Chandrasekaran, S.; Choi, D. Synthesis of hierarchically structured  $\gamma$ -Fe<sub>2</sub>O<sub>3</sub>–PPy nanocomposite as effective adsorbent for cationic dye removal from wastewater. *Environ. Pollut.* **2020**, *267*, 115498. [[CrossRef](#)] [[PubMed](#)]
26. Cao, Y.-Q.; Zi, T.-Q.; Zhao, X.-R.; Liu, C.; Ren, Q.; Fang, J.-B.; Li, W.-M.; Li, A.-D. Enhanced visible light photocatalytic activity of Fe<sub>2</sub>O<sub>3</sub> modified TiO<sub>2</sub> prepared by atomic layer deposition. *Sci. Rep.* **2020**, *10*, 13437. [[CrossRef](#)] [[PubMed](#)]
27. Liu, Y.; Sun, N.; Hu, J.; Li, S.; Qin, G. Photocatalytic degradation properties of  $\alpha$ -Fe<sub>2</sub>O<sub>3</sub> nanoparticles for dibutyl phthalate in aqueous solution system. *R. Soc. Open Sci.* **2018**, *5*, 172196. [[CrossRef](#)] [[PubMed](#)]
28. Liu, B.; Wang, D.; Li, H.; Xu, Y.; Zhang, L. As(III) removal from aqueous solution using  $\alpha$ -Fe<sub>2</sub>O<sub>3</sub> impregnated chitosan beads with As(III) as imprinted ions. *Desalination* **2011**, *272*, 286–292. [[CrossRef](#)]
29. Arshad, N.; Ahmed, I.; Irshad, M.S.; Li, H.R.; Wang, X.; Ahmad, S.; Sharaf, M.; Firdausi, M.; Zaindin, M.; Atif, M. Super Hydrophilic Activated Carbon Decorated Nanopolymer Foam for Scalable, Energy Efficient Photothermal Steam Generation, as an Effective Desalination System. *Nanomaterials* **2020**, *10*, 2510. [[CrossRef](#)]
30. Kabeel, A.E.; El-Agouz, S.A. Review of researches and developments on solar stills. *Desalination* **2011**, *276*, 1–12. [[CrossRef](#)]
31. Schön, S.J. Chapter 9—Thermal properties. In *Physical Properties of Rocks*; Schön, J.H., Ed.; Handbook of Petroleum Exploration and Production; Elsevier: Amsterdam, The Netherlands, 2011; Volume 8, pp. 337–372.
32. Wang, P.; Gu, Y.; Miao, L.; Zhou, J.; Su, H.; Wei, A.; Mu, X.; Tian, Y.; Shi, J.; Cai, H. Co<sub>3</sub>O<sub>4</sub> nanoforest/Ni foam as the interface heating sheet for the efficient solar-driven water evaporation under one sun. *Sustain. Mater. Technol.* **2019**, *20*, e00106. [[CrossRef](#)]
33. Xue, Y.; Wang, Y. A review of the  $\alpha$ -Fe<sub>2</sub>O<sub>3</sub> (hematite) nanotube structure: Recent advances in synthesis, characterization, and applications. *Nanoscale* **2020**, *12*, 10912–10932. [[CrossRef](#)]
34. Chen, Q.; Pei, Z.; Xu, Y.; Li, Z.; Yang, Y.; Wei, Y.; Ji, Y. A durable monolithic polymer foam for efficient solar steam generation. *Chem. Sci.* **2018**, *9*, 623–628. [[CrossRef](#)]
35. Xiao, C.; Chen, L.; Mu, P.; Jia, J.; Sun, H.; Zhu, Z.; Liang, W.; Li, A. Sugarcane-Based Photothermal Materials for Efficient Solar Steam Generation. *ChemistrySelect* **2019**, *4*, 7891–7895. [[CrossRef](#)]
36. Huang, W.; Hu, G.; Tian, C.; Wang, X.; Tu, J.; Cao, Y.; Zhang, K. Nature-inspired salt resistant polypyrrole–wood for highly efficient solar steam generation. *Sustain. Energy Fuels* **2019**, *3*, 3000–3008. [[CrossRef](#)]

37. Yu, F.; Chen, Z.; Guo, Z.; Irshad, M.S.; Yu, L.; Qian, J.; Mei, T.; Wang, X. Molybdenum Carbide/Carbon-Based Chitosan Hydrogel as an Effective Solar Water Evaporation Accelerator. *ACS Sustain. Chem. Eng.* **2020**, *8*, 7139–7149. [[CrossRef](#)]
38. Yu, F.; Guo, Z.; Xu, Y.; Chen, Z.; Irshad, M.S.; Qian, J.; Mei, T.; Wang, X. Biomass-Derived Bilayer Solar Evaporator with Enhanced Energy Utilization for High-Efficiency Water Generation. *ACS Appl. Mater. Interfaces* **2020**, *12*, 57155–57164. [[CrossRef](#)]
39. Xu, Y.; Wang, J.; Yu, F.; Guo, Z.; Cheng, H.; Yin, J.; Yan, L.; Wang, X. Flexible and Efficient Solar Thermal Generators Based on Polypyrrole Coated Natural Latex Foam for Multimedia Purification. *ACS Sustain. Chem. Eng.* **2020**, *8*, 12053–12062. [[CrossRef](#)]
40. Parsa, S.M.; Rahbar, A.; Koleini, M.H.; Aberoumand, S.; Afrand, M.; Amidpour, M. A renewable energy-driven thermoelectric-utilized solar still with external condenser loaded by silver/nanofluid for simultaneously water disinfection and desalination. *Desalination* **2020**, *480*, 114354. [[CrossRef](#)]
41. Zong, L.; Li, M.; Li, C. Intensifying solar-thermal harvest of low-dimension biologic nanostructures for electric power and solar desalination. *Nano Energy* **2018**, *50*, 308–315. [[CrossRef](#)]
42. Wang, C.; Wang, J.; Li, Z.; Xu, K.; Lei, T.; Wang, W. Superhydrophilic porous carbon foam as a self-desalting monolithic solar steam generation device with high energy efficiency. *J. Mater. Chem. A* **2020**, *8*, 9528–9535. [[CrossRef](#)]
43. Qin, D.-D.; Zhu, Y.-J.; Yang, R.-L.; Xiong, Z.-C. A salt-resistant Janus evaporator assembled from ultralong hydroxyapatite nanowires and nickel oxide for efficient and recyclable solar desalination. *Nanoscale* **2020**, *12*, 6717–6728. [[CrossRef](#)] [[PubMed](#)]
44. Shan, X.; Lin, Y.; Zhao, A.; Di, Y.; Hu, Y.; Guo, Y.; Gan, Z. Porous reduced graphene oxide/nickel foam for highly efficient solar steam generation. *Nanotechnology* **2019**, *30*, 425403. [[CrossRef](#)] [[PubMed](#)]
45. Yang, L.; Li, N.; Guo, C.; He, J.; Wang, S.; Qiao, L.; Li, F.; Yu, L.; Wang, M.; Xu, X. Marine biomass-derived composite aerogels for efficient and durable solar-driven interfacial evaporation and desalination. *Chem. Eng. J.* **2020**, *417*, 128051. [[CrossRef](#)]
46. Parsa, S.M.; Rahbar, A.; Koleini, M.H.; Davoud Javadi, Y.; Afrand, M.; Rostami, S.; Amidpour, M. First approach on nanofluid-based solar still in high altitude for water desalination and solar water disinfection (SODIS). *Desalination* **2020**, *491*, 114592. [[CrossRef](#)]
47. Irshad, M.S.; Arshad, N.; Wang, X.; Li, H.R.; Javed, M.Q.; Xu, Y.; Alshahrani, L.A.; Mei, T.; Li, J. Intensifying solar interfacial heat accumulation for clean water generation excluding heavy metal ions, and oil emulsions. *Sol. RRL* **2021**, *5*, 2100427. [[CrossRef](#)]